Nature Communications

https://doi.org/10.1038/s41467-026-70871-9

Article in Press

Aptamers with magnetically tunable affinity for divalent cobalt ions

Received: 11 October 2025

Accepted: 6 March 2026

Cite this article as: Gao, S., Wang, L., Yao, L. *et al.* Aptamers with magnetically tunable affinity for divalent cobalt ions. *Nat Commun* (2026). https://doi.org/10.1038/s41467-026-70871-9

Shengjie Gao, Lu Wang, Lili Yao, Yu Mao, Michael Eisenstein, Hyongsok Tom Soh & Lei Zheng

Title: Aptamers with Magnetically Tunable Affinity for Divalent Cobalt Ions

Authors: Shengjie Gao[1], Lu Wang[1,2,*], Lili Yao[1], Yu Mao[1], Michael Eisenstein[3,4], Hyongsok Tom Soh[3,4,*], Lei Zheng[1,5,*]

Affiliations:

[1]School of Food and Biological Engineering, Hefei University of Technology, Hefei 230009, China.

[2]Engineering Research Center of Bioprocess, Ministry of Education, Hefei University of Technology, Hefei, 230009, China.

[3]Department of Electrical Engineering, Stanford University, Stanford, CA 94305, United States.

[4]Department of Radiology, Stanford University, Stanford, CA 94305, United States.

[5]Intelligent Interconnected Systems Laboratory of Anhui Province, Hefei University of Technology, Hefei 230009, China.

* Corresponding authors.

Hefei University of Technology, Hefei, 230009, Anhui, P. R. China, and Stanford University, Stanford, CA 94305

E-mail: wanglu@hfut.edu.cn (L. Wang), tsoh@stanford.edu (H. T. Soh), lzheng@hfut.edu.cn (L. Zheng).

Abstract: There is considerable interest in the ability to modulate biological processes with magnetic fields. Here we demonstrate a strategy for selecting aptamers that exhibit enhanced binding to paramagnetic metal ions under a strong magnetic field. Using a high-magnetic-field (HM)-SELEX method targeting Co^{2+}, we identified two classes of aptamers with magnetically-modulated binding behavior. One displayed a gradual 2–3-fold increase in affinity as magnetic field strength increased, while the other went from minimal target binding at ambient field strength to an affinity of ~200 μM at ≥ 6 T. Molecular simulations revealed that the magnetic field induces a global conformational rearrangement by enhancing aptamer-metal electrostatic interactions, optimizing the coordination geometry of the nucleotides. Chemical footprinting and mutational analysis confirmed the role of certain conformational changes in magnetically-induced ion binding. These results suggest opportunities to generate aptamer switches that can be used to manipulate biorecognition processes via an externally applied magnetic field in diverse applications.

Introduction

A number of groups are currently exploring the use of magnetic fields as a means for controlling biological processes. For example, the emerging field of magnetogenetics entails the identification of magnetically-responsive proteins and the development of strategies for the remote, noninvasive manipulation of neuronal function[1]. In 2015, the Xie group identified MagR, a naturally occurring magnetosensor protein that aligns with weak geomagnetic fields (~50 μT), which could potentially prove useful as a tool for magnetically actuating physiological functions[2]. However, this finding remains contentious. Some critics argue that the proposed mechanism faces significant physical challenges, particularly regarding thermal noise ($k_BT = 4 \times 10^{-21}$ J) damping effects on the interaction energy ($mB_{Earth} = 1 \times 10^{-25}$ J) of small magnetic moments in weak magnetic fields[3,4]. In other theoretical calculations of magnetic force and magnetic heating, the forces, torques, or temperatures they produce are too small by several orders of magnitude (~10^5-10^{10}) for the desired effects on molecular orientation or membrane channels[3]. Despite this ongoing debate, the broader possibility of using magnetic fields as an external trigger for biological processes remains intriguing, even if the feasibility of implementing such actuation strategies is still underexplored.

Metal ions from the first transition series (*e.g.,* Fe^{2+}, Co^{2+}, or Ni^{2+}) often display unusual behavior in magnetic fields due to their unpaired 3d orbital electrons. These metal ions are known to bind to proteins and are vital for sustaining life—for example, these and other metal ions act as cofactors for many enzymes and are also involved in transporting vital substances like oxygen. Nucleic acids also exhibit very high affinity for metal ions, driven by interactions between metal cations and the negatively-charged

phosphate backbone as well as coordination with donor atoms of the nucleobases[5–7]. For example, binding between certain riboswitches and paramagnetic metal ions like Co^{2+}, Ni^{2+}, or Mn^{2+} can induce structural changes that regulate gene expression[8–10]. Researchers have also used *in vitro* screening to generate a variety of aptamers and DNAzymes capable of sequence-specific DNA interactions with metal ions[11–13]. The intrinsic magnetic sensitivity of these ions and feasibility of engineering external controllability into *in vitro* screening procedures provide a unique opportunity to transform metal-binding aptamers into magnetically-actuated molecular switches.

In this work, we isolate magnetic field-responsive Co^{2+}-binding DNA aptamers using a graphene oxide (GO)-SELEX method under a 9 T static field, which is 180,000 times stronger than the Earth's geomagnetic field. Our 'HM-SELEX' method employs positive selection under a high-flux magnetic field and counter-selection under ambient magnetic field conditions. GO efficiently removes unbound single-stranded DNA via π-π stacking, enriching switches with magnetic field-dependent affinity. We identify two distinct classes of magnetically-responsive aptamers from this process. The first class binds Co^{2+} under ambient conditions, but exhibits greater affinity at 9 T, with a 2–3-fold decrease in its equilibrium dissociation constant (K_d) from 171 μM to 48.7 μM. In contrast, the second class of aptamers displays negligible affinity in ambient conditions but achieves a K_d for Co^{2+} of ~200 μM under high magnetic fields (≥ 6 T). We reveal that magnetic fields enhance the electrostatic forces between the aptamer and Co^{2+}, inducing global conformational rearrangements that optimize the coordination geometry. These reversible structural changes enable magnetic control of the binding affinity.

To the best of our knowledge, this work represents the first demonstration of functional coupling

between aptamer binding affinity and magnetic field strength. Such aptamers could enable programmable applications including smart MRI contrast switches[14–16], magnetic field-activated drug release[17], stimulus-responsive functional materials[18,19], and magnetically-induced gene editing[20].

Results

Aptamer screening under a high magnetic field

We designed our HM-SELEX screening strategy—based on the GO-SELEX method[21]—to enable the selective isolation of ion-specific aptamers whose affinities can be modulated by magnetic field strength. Although conventional capture-SELEX is indeed a mature method and often yields strong enrichment[22], it is incompatible with our 9 T screening setup. Under high static magnetic fields, commonly used stationary phases such as magnetic beads become strongly magnetized and aggregate, disrupting the screening environment's uniformity and introducing uncontrollable variables. We therefore employed GO-SELEX, a homogeneous solution-phase method that minimizes surface immobilization and steric constraints. This ensures that aptamer selection is driven primarily by Co^{2+}–aptamer interaction under magnetic field modulation. HM-SELEX involves performing positive selection under a steady high (9 T) magnetic field, combined with a counter-selection process performed under the ambient geomagnetic field ($\leq 5\times10^{-5}$ T) (Fig. 1). In this study, we chose the paramagnetic cobalt(II) ion as our primary target; Co^{2+} is intrinsically responsive to high magnetic fields due to its substantial permanent magnetic moment, which arises from three unpaired electrons in its high-spin state.

We used a single-stranded (ss) DNA library consisting of a 40-nt random region flanked by 20-nt forward and reverse PCR primer sites, with a FAM fluorophore label at the 5' end. Positive selection was

performed under a steady 9 T field, using GO to efficiently partition unbound sequences (optimization details in Supplementary Fig. 1). Crucially, to ensure both ion specificity and magnetic dependence, we implemented a stringent dual counter-selection regime. This step actively eliminated sequences that bound interfering metal ions at 9 T, as well as those capable of binding Co^{2+} under ambient geomagnetic conditions. Consequently, only aptamers displaying specific, high-field-induced affinity were retained for amplification.

As a demonstration, we performed seven rounds of selection for Co^{2+} with progressively increasing stringency (Supplementary Table 1). Monitoring the library recovery rate revealed a characteristic enrichment profile. After an initial rise, the introduction of counter-selection in Round 4 caused a sharp decline to 3.75%, effectively removing non-specific binders. By Round 7, recovery rebounded to 56.7%, indicating the dominance of high-affinity sequences (Supplementary Fig. 2). High-throughput sequencing of this final pool yielded 3,142,315 reads. The ten most abundant sequences (representing ~1.00% of total reads) were selected for further validation based on their enrichment trends in the final-round library.

Aptamer-ion affinity under high magnetic field

We evaluated the affinity of the isolated aptamers against Co^{2+} using a GO-based fluorescence assay previously reported in Ref. [23] with slight modifications. Briefly, FAM-labeled aptamers were incubated with varying concentrations of Co^{2+} under either a steady 9 T magnetic field or the ambient magnetic field. GO was then introduced to quench the fluorescence of the unbound fraction of FAM-labeled aptamers, and the remaining fluorescence—representing the bound fraction of aptamer—was plotted as a function of Co^{2+} concentration to determine the K_d. The initial library did not show substantial affinity for Co^{2+}

under either the 9 T field or the ambient magnetic field (Supplementary Fig. 3).

Under ambient geomagnetic conditions, we determined the affinities of the top ten aptamers (named Co-M1 to M10). Five aptamers (Co-M1, -M2, -M3, -M4, and -M9) exhibited measurable binding to Co^{2+}, with K_d of 50–250 μM (Fig. 2a). This represents a notable improvement in affinity compared to existing RNA aptamers for Co^{2+}, which typically exhibit K_d values in the millimolar range[13]. Interestingly, the binding affinities of these sequences were further enhanced by ~2–3-fold under a steady 9 T magnetic field. We also found that the K_d of Co-M3 gradually decreased from 171 μM to 50 μM as the magnetic field strength increased to 3, 6, and 9 T, indicating that its affinity could be tuned by the strength of the magnetic field (Fig. 2b). A recently reported DNA aptamer achieves a higher intrinsic affinity (K_d < 3 μM), but this sequence exhibits relatively lower specificity and binds broadly across first-row transition metals[24].

We utilized isothermal titration calorimetry (ITC) to determine the binding thermodynamics (ΔH, ΔS, ΔG) and stoichiometry (n) between Co-M3 and Co^{2+}. These parameters in turn revealed conformational rearrangement and solvation effects during the binding process[25,26]. These measurements were performed only under ambient magnetic field conditions due to limitations of the instrument. Co-M3 exhibited a K_d of 15.10 ± 4.15 μM, which is ~10-fold lower than what we measured from the GO-based fluorescence assay. The lower K_d value measured by ITC was predictable, given that the GO-based fluorescence assay relies on adsorption competition to determine aptamer affinity. The addition of Co^{2+} resulted in an exothermic thermogram and revealed a stoichiometric ratio of about 10:1. The exothermic enthalpy (ΔH = −9.07 kcal/mol) and negative entropic change (TΔS = −2.49 kcal/mol) observed in ITC (Fig. 2c) indicate

that Co^{2+}-Co-M3 binding is driven by electrostatic and hydrogen-bonding interactions rather than hydrophobic effects[27,28]. We also performed circular dichroism (CD) spectroscopy, and found that Co-M3 displayed a noticeable shift in peak position upon introduction of Co^{2+} under the ambient magnetic field, indicating strong specific binding to Co^{2+} and a conformational shift (Fig. 2d).

The other five sequences from the top ten (Co-M5, -M6, -M7, -M8, and -M10) showed negligible Co^{2+} affinity under ambient conditions. However, two of these sequences (Co-M8 and -M10) exhibited a K_d of ~200 μM under a 9 T magnetic field (Fig. 3a–c and Supplementary Fig. 4). When we tested the performance of Co-M8 under incrementally increased magnetic field strengths, we only saw measurable Co^{2+} binding when the field exceeded a threshold of 6 T (Fig. 3b). We also characterized Co-M8 binding to Co^{2+} under ambient conditions using ITC and CD spectroscopy (Fig. 3d, e). ITC measurements confirmed that Co-M8 does not exhibit meaningful binding under ambient magnetic conditions. CD spectrometry also showed no conformational change in the presence of a 10-fold molar excess of Co^{2+}. These results suggest that Co-M8 may be a true magneto-responsive aptamer switch that only shows affinity for Co^{2+} at magnetic fields ≥ 6 T. Furthermore, kinetic analysis was performed by incubating Co-M8 (25 nM) with Co^{2+} (300 μM) in the bore of a 9 T magnet and quantifying binding over 0–60 min using a time-resolved GO-quenching fluorescence readout (GO added immediately to each aliquot; centrifugation and supernatant fluorescence measurement); the fluorescence reached a plateau at approximately 30 min (Supplementary Fig. 5). These relatively slow kinetics are consistent with a global conformational rearrangement and the cooperative assembly of a multi-ion coordination cluster[29]. We further distinguished this specific multi-ion cluster from the non-specific “M-DNA” phase transition,

which refers to a non-canonical DNA structure where divalent metal ions replace the imino protons of base pairs—a process that typically occurs at elevated pH (pH > 8.0) and results in a densely packed helix that excludes intercalating dyes[30,31]. Unlike M-DNA formation, our aptamer complex shows pH-independent Co^{2+} binding and remains accessible to ethidium bromide intercalation (Supplementary Fig. 6).

We further validated the magnetic field-dependent affinity enhancement for both Co-M3 and Co-M8 by quantifying the bound aptamer fractions using polyacrylamide gel electrophoresis (PAGE) (Supplementary Fig. 7). Under a 9 T magnetic field, Co-M3 bands appeared at lower target concentrations (about 30 μM) and reached saturation more rapidly (≥ 100 μM); in contrast, at ambient conditions, these bands only started to appear at Co^{2+} concentrations > 150 μM, confirming greatly reduced binding affinity. For Co-M8, bands were not visible at all under ambient conditions, but displayed concentration-dependent intensity at 9 T.

To validate these findings and provide spectroscopic evidence of field-dependent structural rearrangements, we further characterized the representative aptamers Co-M3 and Co-M8 using two GO-free methods. First, we employed a strand-displacement assay in which the aptamer was 5′-FAM-labeled and challenged by a short 3′-BHQ1-labeled complementary DNA (cDNA, 20 nt) designed to hybridize to the 5′ terminal primer-binding region immediately adjacent to the FAM label. In this construct, cDNA binding places BHQ1 in proximity to FAM and quenches fluorescence; however, target-ion binding stabilizes the folded aptamer, reducing cDNA strand displacement and preserving FAM fluorescence. Immediately following incubation, samples were transferred for rapid fluorescence acquisition to

minimize any post-incubation conformational changes. For Co-M3, the K_d improved from 269 μM under ambient conditions to 113 μM under the 9 T field (~2.4-fold enhancement). Consistent with its switching behavior, Co-M8 transitioned from negligible binding in the ambient field to a K_d of 228 μM at 9 T (Supplementary Fig. 8).

Second, Förster resonance energy transfer (FRET) measurements confirmed that these affinity shifts are driven by magnetically-modulated conformational changes. The sequences were synthesized with a 5'-FAM donor and a 3'-TAMRA acceptor. In this dual-labeled construct, Co^{2+}-induced folding decreases the end-to-end distance, producing a FRET response that was quantified as the emission ratio (F_{580}/F_{518}) and fit to obtain apparent K_d values. Consistent with our other spectroscopic protocols, samples were immediately transferred for rapid fluorescence acquisition following a 30-min incubation under ambient or 9 T fields to preserve the field-stabilized structures. Under ambient conditions, Co-M8 exhibited negligible changes in FRET signal even at high Co^{2+} concentrations, indicating a lack of folding. In contrast, samples incubated under the 9 T field displayed a concentration-dependent structural transition, yielding a K_d of 114 μM. Similarly, while Co-M3 underwent conformational changes in both conditions, the presence of the 9 T field induced a significantly sharper response and higher apparent affinity (43.1 μM) compared to the ambient control (217 μM). As a control, we also measured the initial library, which showed no affinity under either magnetic field (Supplementary Fig. 9).

We next characterized the specificity of Co-M3 and -M8 to 300 μM Co^{2+} versus a 10-fold greater concentration of non-target ions (*i.e.,* Mn^{2+}, Cu^{2+}, Ca^{2+}, Al^{3+}, Ba^{2+}, Cd^{2+}, Ni^{2+}, Zn^{2+}, Ce^{3+}, Pb^{2+}, Cr^{3+}, Fe^{3+}, and Hg^{2+}) using the GO-based fluorescence assay. Co-M3 predictably displayed strong Co^{2+} binding in

both magnetic field conditions, whereas Co-M8 only bound strongly to Co^{2+} under high magnetic field conditions (Fig. 4). Both aptamers generally demonstrated good selectivity against non-target ions, with the notable exception of Hg^{2+}. This Hg^{2+} interference likely stems from the exceptionally strong interaction between Hg^{2+} and thymine bases, which appears to dominate over the Co^{2+}-specific recognition elements in the aptamer structure. We also observed that the binding of these two aptamers to Hg^{2+} was not affected by magnetic fields. Nevertheless, this off-target binding to Hg^{2+} may require us to introduce more rigorous counter-selection processes in future work.

To further elucidate the functional characteristics of the sequences obtained during our HM-SELEX screening process, we analyzed the 500 most abundant sequences (representing ~3.94% of all 3,142,315 reads) from the final round for recurring sequence motifs using the motif discovery tool in the MEME suite (version 5.5.7)[32]. We found four different motifs (E-value < 0.05), M1–4, which appeared with the following frequencies: M1 in 437/500 (87.4%), M2 in 148/500 (29.6%), M3 in 73/500 (14.6%), and M4 in 25/500 (5.0%) of sequences (Supplementary Fig. 10). We subsequently analyzed the motif composition of the 10 most abundant aptamer sequences (Fig. 5a) and predicted their secondary structure (Supplementary Fig. 11). Motif M1 was found in all 10 sequences; four also contained M2, and three contained M3 (Fig. 5b). Notably, even though all 10 sequences contained the M1 motif, their predicted secondary structures were notably different. As examples, we have analyzed three of these sequences, Co-M3, -M5, and -M8 (Fig. 5c–e). Co-M3 contains M1 and M3 and exhibits multiple small stem-loops distributed around the main loop structure. Co-M5 contains a similar main structure to Co-M3 but contains only M1. The M1 region of Co-M8 is partially complementary to a region containing M2 and the 3' primer

sequence, forming a relatively long stem structure that yields a semi-open conformation formed by nucleotides within M1.

Molecular dynamics (MD) simulation of Co^{2+} binding under a high magnetic field

To further explore the effects of the magnetic field on aptamer binding to Co^{2+} ions, we performed MD simulations incorporating the Lorentz force acting on charged particles and the Zeeman effect on particles with magnetic spin. Based on the stoichiometry observed in our ITC results, we introduced 10 Co^{2+} ions into the system under varying magnetic field conditions for both Co-M3 and Co-M8, with initial positions established through conserved sequence analysis and molecular docking. The simulation process commenced with energy minimization and pre-equilibration to establish reasonable initial structures for 10 ns, with a time step of 1 fs. This was followed by a 100-ns NVT production simulation using a 2-fs time step at a temperature of 310 K. The final 50 ns of trajectories were extracted and analyzed across different magnetic field intensities. Co-M3 and -M8 exhibited progressive structural divergence upon Co^{2+} binding as the magnetic field increased from ambient to 9 T (Fig. 6a, b), consistent with our experimental results. Since the overall pre-screening was performed at 9 T, these gradual structural transitions may naturally contribute to enhanced affinity for Co^{2+} under high magnetic fields.

Additionally, we calculated the binding free energy for the full 100-ns trajectory using the Molecular Mechanics/Poisson-Boltzmann Surface Area (MMPBSA) method[33]. The results indicated that the total binding energies of both Co-M3 and -M8 with cobalt ions significantly increase with the strength of the magnetic field (Fig. 6c, d), which is consistent with the affinity trends described above. We performed further decomposition of the total energy, and identified the main energy components, including van der

Waals (vdW) and electrostatic forces (Supplementary Fig. 12). For Co-M3, as the magnetic field increased from ambient to 9 T, the vdW energy increased from 11.27 to 28.11 kcal/mol, while for Co-M8, it changed from 12.27 to 23.44 kcal/mol (~1% of the total energy). In contrast, the electrostatic interaction energy for Co-M3 ranged from -11,939.39 kcal/mol to -22,459.28 kcal/mol; for Co-M8, it ranged from -16,921.24 kcal/mol to -20,940.95 kcal/mol (~99% of the total energy). This is consistent with the thermodynamic parameters (for Co-M3, $\Delta H < 0$ and $\Delta S < 0$) obtained from ITC (Fig. 2c).

We used energy decomposition analysis as calculated by the MMPBSA method to quantify the energetic contributions of individual nucleotides from Co-M3 and M8 in binding to Co^{2+} under varying magnetic field strengths (Supplementary Fig. 13). As the magnetic field strengthens, more nucleobases and Co^{2+} ions participate in the binding process, leading to a consistent rise in interaction energy. The nucleotides with the highest energy contribution came from the conserved motifs within the two aptamers (*e.g.*, A41 from M3 of Co-M3 and G27 from M1 of Co-M8). However, several nucleotides within the non-motif regions and even the primer regions were also involved in binding to Co^{2+}. This multiregional synergy implies that the magnetic field may influence the function of these aptamers by modulating the conformations of their flexible regions.

To examine the influence of the magnetic field on the coordination bonding strength between the aptamer and cobalt ions, we selected the cobalt ions exhibiting the strongest binding interactions with their surrounding pockets—based on energy decomposition—as representative molecules. We then analyzed the coordination structure of Co^{2+} with the surrounding nucleotides. We employed independent gradient model (IGM) analysis using pro-molecular approximation to identify interaction types (*i.e.,*

components) and their spatial distributions. For Co-M3, Co^{2+} binds to oxygen atoms on nucleobases C40 and A41 through strong electrostatic interactions (Fig. 6e). Similarly, for Co-M8, Co^{2+} interacts with oxygen atoms on C26, G27, C66, and G67 (Fig. 6f). The coordination conformations of these correlations changed as the magnetic field increased, with the average distance of the correlated atoms changing more in Co-M3 (from 1.000 to 0.970) and the coordination structure being more stable and less variable in Co-M8 (from 1.000 to 0.990) (Supplementary Table 3).

Magnetic field-dependent conformational remodeling

To provide spectroscopic support for magnetic-field–induced conformational changes, we conducted UV–vis absorption measurements. In these experiments, aptamer–Co^{2+} mixtures were incubated under ambient conditions or a 9 T field, and spectra were then acquired immediately to minimize post-incubation changes (Supplementary Fig. 14). The nucleic acid band at 260 nm, which is sensitive to base stacking and global conformational rearrangement, showed an enhanced Co^{2+}-induced response for Co-M3 after 9 T exposure. In contrast, Co-M8 displayed minimal change under ambient conditions but a clear response after 9 T exposure, consistent with the threshold-like field dependence we observed in functional assays. In addition, the Co^{2+}-associated absorption in the visible region (≈ 500 nm, d–d transition) was enhanced after 9 T incubation for both Co-M3 and Co-M8, supporting a magnetic-field–dependent modulation of the Co^{2+} coordination environment in the presence of the aptamers.

We next experimentally assessed the conformational differences at nucleotide resolution in Co-M8-Co^{2+} binding using $KMnO_4$ reactivity[34,35] (which preferentially modifies thymine) and dimethyl sulfate (DMS) methylation (which preferentially modifies guanine) interference experiments (Supplementary Fig.

15)[36–38]. The cleavage activity of $KMnO_4$ was restricted by base-pairing in the double-stranded structure, enabling the prediction of secondary structure. After addition of the target, conformational changes in the aptamer further alter the reactivity of $KMnO_4$ and DMS, guiding the prediction of binding sites. After denaturing PAGE separation (Supplementary Fig. 15a), the cleavage patterns for Co-M8 were consistent with our predicted secondary structure model, with two stem-loops: P1 consists of 15 nucleotides, while P2 comprises three base-paired regions (P2-1, P2-2, and P2-3) and totals 44 nucleotides (Supplementary Fig. 15d). Comparison of the footprints obtained after binding to Co^{2+} before and after exposure to high magnetic field with those from a Co^{2+}-free control experiment revealed 18 linkages with decreased cleavage and 11 with increased cleavage. We also identified widely distributed binding sites, including motifs M1 and M2 and even parts of the primer region, consistent with our MD simulations. Quantitative analysis of band intensities (Supplementary Fig. 15b, c) revealed enhanced protection of all four sites (7G, 11T, 18G, 20G) in the P1 domain (stem region) at 9 T; P2-1 was further protected at three of four key sites (27G, 63G, 64G), while P2-2 and P2-3 exhibited increased exposure at three of five sites (35T, 36T, 53T) at 9 T.

To further elucidate sequence-structure determinants governing Co^{2+} binding and magnetic sensitivity, we performed point-mutagenesis of selected sites within the P2 stem structure (Fig. 7a), focusing on eight key nucleotides based on the above energy decomposition calculation (maximum binding energy) and chemical footprint analysis (significant changes). These eight bases complementarily pair with the M2 motif or primer region to form a long stem structure, and we introduced mutations that create base mismatches and thereby alter the aptamer conformation. Remarkably, six of the eight mutants—

distributed across P2-1 and P2-2, including C26G, G27T, T35A, T36A, G63T, and G64A—exhibited complete abolition of Co^{2+} binding affinity under both 9 T and ambient magnetic field conditions, indicating that these nucleotides are critical for Co^{2+} recognition. The C52T and T53C mutants were notable exceptions, exhibiting binding affinity comparable to Co-M8 at 9 T under ambient magnetic conditions (K_d = ~200 μM), alongside improved affinity to the original sequence at 9 T (K_d = ~60 μM). ITC analysis confirmed that both variants (Co-M8-C52T and Co-M8-T53C) display well-defined exothermic binding isotherms with high affinity ($K_d \approx 14$ μM) while retaining a reproducible stoichiometry of N ≈ 10 (Supplementary Fig. 16). This conserved stoichiometry supports a specific multi-ion coordination cluster as the functional unit underlying the magnetically-driven conformational switch, rather than nonspecific binding. Secondary structure analysis revealed that this single mutation disrupts the P2-3 stem structure (Fig. 7b), consistent with our footprinting data showing increased exposure of P2-3 nucleotides at 9 T. These results suggest that the activation of the affinity of the Co-M8 sequence for Co^{2+} under high magnetic fields is informed by the conformational transition of P2-3.

Discussion

In this study, we report a screening process that enabled us to isolate, to the best of our knowledge, the first examples of DNA aptamers that exhibit magnetically tunable target-binding properties. Using Co^{2+} as a model target, we isolated two distinct classes of Co^{2+}-binding aptamers through our HM-SELEX approach under a high magnetic field (9 T) along with stringent counter-selection. We identified two sets of aptamers with distinctive magnetic field-dependent behaviors: one exhibiting a ~2–3-fold affinity

enhancement at 9 T compared to ambient conditions, while the other only exhibits target binding under magnetic field strengths of $\geqslant$6 T.

Based on our experimental and MD simulation results, we propose that the magnetic field-responsive affinity of Co^{2+}-targeting aptamers originates from coordination optimization. Previous studies indicate that nucleic acid-Co^{2+} binding occurs through coordination with phosphate groups and nucleobases, enabled by spatial alignment with vacant 3d orbitals [7,39]. Notably, the three unpaired 3d electrons of Co^{2+} are magnetically sensitive, such that external magnetic fields can perturb their electron distribution and thereby modulate ligand accessibility. This is suggested by the magnetically-enhanced interaction energy profiles between Co^{2+} and the surrounding pocket (Fig. 6c, d). Additionally, energy decomposition analysis indicates that >99% of the binding energy arises from aptamer-metal electrostatic interactions (*i.e.*, coordination bonding; Fig. 6e, f). Aptamers with certain structures may achieve optimized coordination geometry through electrostatic interactions with Co^{2+} in which they undergo global conformational changes (Fig. 6a, b) that expose cryptic binding pockets (*e.g.*, P2-3 in Co-M8), as evidenced by chemical footprinting (Supplementary Fig. 15) and mutagenesis experiments (Fig. 7), resulting in enhanced affinity in a high magnetic field.

The field effect only needs to account for a small free-energy shift. A two-fold change in K_d corresponds to $\Delta\Delta G = RT \ln 2 \approx 1.7$ kJ mol^{-1} (298 K). In contrast to the full binding free energy ($\Delta G \approx -27.6$ kJ mol^{-1} from ITC), the maximum Zeeman energy of a high-spin Co^{2+} ion at 9 T is on the order of 10^{-21} J per ion ($\approx$ 0.15 kJ mol^{-1}). Given an apparent stoichiometry of ~10 Co^{2+} per aptamer, the collective

magnetic energy (~1.5 kJ mol^{-1}) becomes comparable to $\Delta\Delta G$. This quantitative agreement suggests the magnetic field acts as a sufficient thermodynamic bias to modulate the binding equilibrium.

To rigorously validate that the observed field-dependent energy stabilization is specific to the paramagnetic properties and not an artifact of the simulation setup, we performed parallel control simulations using a diamagnetic metal ion (Hg^{2+}). We selected Hg^{2+} because our experimental data indicated that it binds strongly to Co-M3 and -M8 but exhibits no magnetic responsiveness. Under identical simulation protocols, the interaction energy profiles of Co-M3 and -M8 binding to Hg^{2+} exhibited only stochastic fluctuations with no systematic divergence or enhancement trend across magnetic fields ranging in strength from ambient conditions to 9 T (Supplementary Fig. 17). This stands in sharp contrast to the monotonic energetic stabilization observed for Co^{2+} (Fig. 6c, d, and Supplementary Fig. 12).

Magnetic fields are known to influence diverse biological processes, including protein function[40,41], cell proliferation[42], differentiation[43], and neuronal stimulation[44,45]. However, the molecular mechanisms behind these effects remain poorly understood. Current engineering strategies for magnetic modulation are generally focused on magnetogenetic systems that couple magnetic stimuli to genetically-encoded protein machinery[46], or magnetic plasma biosensors, which primarily function by enhancing a readout signal through the manipulation of optical and magneto-optical effects in magnetic metallic nanostructures[47]. In this study, we report the active selection of molecular switches that respond directly to magnetic fields. This phenomenon involves the interaction of paramagnetic ions with unpaired electrons, a mechanism that could provide the basis for magnetosensitivity in other biological systems.

These findings offer potential avenues for manipulating biorecognition with external magnetic stimuli. Crucially, unlike protein-based magnetosensors, which often require complex expression systems, DNA aptamers are chemically synthesized, easily modified, and highly programmable, enabling their direct integration into biosensors for the magnetic modulation of binding events.

However, several limitations remain. The magnetic field effects observed here were limited to Co^{2+}, a paramagnetic ion with unpaired electrons. In contrast, our attempts to generate magnetically-responsive aptamers for Hg^{2+} were unsuccessful (see Supplementary Note 1, Supplementary Fig. 18–21). This seems to imply that the current version of the method is exclusively suitable for the screening of magnetically-sensitive aptamers for paramagnetic metal ion targets.

To determine if magnetic responsiveness is an intrinsic property of Co^{2+}-binding aptamers, we tested a previously reported high-affinity DNA aptamer (Co-1) selected under ambient conditions[24]. This aptamer has been reported to bind Co^{2+} with 1:1 stoichiometry and a $K_d < 3$ μM. Using two orthogonal assays (GO-based fluorescence and strand displacement), we found that the control aptamer Co-1 exhibited no measurable difference in affinity under ambient or 9 T magnetic fields (see Supplementary Note 2, Supplementary Fig. 22). These results indicate that high intrinsic affinity for a paramagnetic ion does not guarantee magnetic responsiveness, supporting the conclusion that magnetic sensitivity is a distinct trait enriched by HM-SELEX, which we attribute to the multi-ion coordination architecture of our selected aptamers.

In addition, it would be advantageous if we could lower the threshold of the magnetic field switching effect to meet field-strength thresholds suitable for practical applications—for example, clinical MRI

instruments usually operate in the range of 1.5–3 T. Despite these limitations, this study provides proof of concept for the development of magnetic field-responsive molecular tools. Through rational design of aptamer-paramagnetic ion pairs, it should be feasible to achieve more sensitive magnetic control-based biological recognition systems in the future.

Methods

Oligonucleotides and other materials

All DNA oligonucleotides (see Supplementary Table 4 for sequences), including ssDNA libraries, primers and selected aptamer sequences, were synthesized and purified by Sangon Biotech. High-capacity Magne streptavidin beads were acquired from Promega. Graphene oxide (GO) was purchased from XFNANO Technology. $CoCl_2 \cdot 6H_2O$ and other metal ion salts were purchased from Aladdin Reagent Company. Hg^{2+} ion standard solution was purchased from Guobiao Testing & Certification. All other chemicals were ordered from Sigma-Aldrich. Ultrapure water was produced by the Milli-Q system (18.2MΩ, Millipore Sigma).

Optimization of GO adsorption conditions for the ssDNA library

GO was added to the FAM-labeled ssDNA library in 400 μL reaction buffer (50 mM HEPES, 100 mM NaCl, 0.025% Tween-20, pH 7.5) in varying ratios (GO:ssDNA ratio = 0, 0.4, 0.8, 1.2, 2.4, 3.2, 4.0 μg/pmol). After mixing well, the tubes were incubated at room temperature for 30 min, followed by centrifugation at 15,173 x *g* for 5 min. Similarly, different incubation times (0, 10, 20, 30, 40, 60 min) were investigated to establish minimum quenching times. The fluorescence intensities of the supernatants were quantified using a microplate reader at an excitation wavelength of 485 nm and emission wavelength of 518 nm, facilitating the calculation of adsorption efficiencies.

HM-SELEX screen for Co^{2+} aptamers

Screening and sample measurement were conducted in a superconducting steady high magnetic field facility (SM1, superconducting magnet) capable of generating static magnetic fields up to 9 T in the

vertical direction. The incubation chamber temperature was maintained at room temperature (approximately 300 K). The magnetic field homogeneity was better than 10% over an axial range of ± 5 cm from the center of the 100-mm-diameter bore. After the magnetic field reached its target intensity, the samples were lifted to the specified height by an external support platform and fixed in place.

Prior to each round of selection, libraries were dissolved in binding buffer (50 mM HEPES, 100 mM NaCl, 0.025% Tween-20, pH 7.5). The library was heated at 95 ℃ for 10 min, cooled on ice for 10 min, and then placed at room temperature for 10 min. The denatured library was incubated with Co^{2+} at steady high magnetic field under conditions described in Supplementary Table 1. GO solution was added to remove unincorporated ssDNA, and the mixture was again incubated under a steady high magnetic field. We centrifuged the mixture at 15,173 x *g* for 5 min to remove the unbound ssDNA library and GO. The recovered ssDNA library was concentrated by ethanol precipitation and PCR amplified with the following conditions: 3 min at 95 °C; 15–25 cycles of 95 °C for 30 s, 50 °C for 30 s, and 72 °C for 60 s; and 3 min at 72 °C. We incubated the PCR products with streptavidin magnetic beads for 60 min to capture dsDNA. After DNA loading, the magnetic beads were washed three times with binding buffer. We added 50 μL of 0.2 M NaOH and incubated for 3 min. The elute containing the library chain was collected and neutralised with 10 μL of 1 M HCl.

We introduced counter-selection in later rounds, counter-selection was performed by incubating the library with an equimolar mixture of interfering ions (300 μM each of Mn^{2+}, Cu^{2+}, Ca^{2+}, Al^{3+}, Ba^{2+}, Cd^{2+}, Ni^{2+}, Zn^{2+}, Ce^{3+}, Pb^{2+}, Cr^{3+}, Fe^{3+} and Hg^{2+}) under a 9 T field. The mixtures were then added to the GO solution for incubation and centrifuged at 15,173 x *g* for 5 min to remove the supernatant. After washing

the precipitate four times with binding buffer, Co^{2+} was added to the precipitate and incubated under ambient conditions. Finally, we centrifuged the mixture at 15,173 x *g* for 5 min, discarded the supernatant, and washed the precipitate four times with binding buffer. We then added fresh Co^{2+} to the mixture and incubated at 9 T. After incubation, we added the GO solution and centrifuged at 15,173 x *g* for 5 min to remove the unbound ssDNA library and GO. The recovered ssDNA library was concentrated by ethanol precipitation and amplified to rebuild the ssDNA library. After seven rounds of selection, the enriched ssDNA library was cloned and sequenced.

HM-SELEX Screen for Hg^{2+} aptamers

The primary difference relative to the Co^{2+} selection involved the binding buffer, which was 1× PBSMT buffer (136.89 mM NaCl, 2.67 mM KCl, 8.1 mM Na_2HPO_4, 1.76 mM KH_2PO_4, 1 mM $MgCl_2$, 0.025% Tween-20, pH 7.4). Other experimental procedures were consistent with the Co^{2+} screening protocol. Specific selection conditions are described in Supplementary Table 2. After eight rounds of selection, the enriched ssDNA library was cloned and sequenced by NovaSeq 6000.

Structural analysis of aptamers and molecular dynamics simulations

The secondary structure of the aptamers was generated using the Mfold web server[48], and the most prevalent three-dimensional conformations of the corresponding aptamers were predicted using 3dRNA/DNA software[49,50]. Binding sites for Co^{2+} were identified through conserved sequence analysis and molecular docking studies. Before the simulation, the simulation space was expanded by an additional 2 nm along all three axes to accommodate the outermost regions of the nucleic acid. This extended space was then filled with water at a concentration of 1 g/mL and charge-neutralized with counter ions (Cl^-).

The General Amber Force Field (GAFF) was applied to the molecules, and the TIP3P water model was utilized to represent water molecules in the MD simulation. The parameters for target ions were specifically adopted from Ref. 51.

All simulations were conducted using the Large-scale Atomic/Molecular Massively Parallel Simulator (LAMMPS) software package[52]. To facilitate simulations under varying magnetic field intensities, we developed several program modules to enhance the original program's functionality. First, for any charged particle, an additional Lorentz force $\vec{F}$ was calculated by

$$\mathbf{F} = q(\mathbf{v} \times \mathbf{B}) \quad (1)$$

where q is the charge of the particle, $\mathbf{v}$ is the velocity of the charged particle, $\mathbf{B}$ is the applied magnetic field vector. This value was then included in the total force acting on the particle, and the particle's velocity and position were then updated accordingly. Second, for particles with magnetic spin, the Zeeman effect was taken into account. This involves calculating the Hamiltonian quantity H_{zeeman} as

$$H_{zeeman} = -g \sum_{i=0}^{N} \mu_i \mathbf{s_i} \times \mathbf{B} \quad (2)$$

in which g denotes the Lande factor, μ_i is the momentum of the spin particle, $\mathbf{s_i}$ is the You vector in the spin direction, and $\mathbf{B}$ is the applied magnetic field vector. These modules were developed using the LAMMPS package, and both unit tests and systematic tests were performed to validate the accuracy of the physical results and ensure the program's robustness.

The simulation process commenced with energy minimization and pre-equilibration to establish reasonable initial structures. A pre-equilibration NPT simulation was conducted for 10 ns with a time step of 1 fs, during which the system's volume and pressure converged. This was followed by a 100-ns NVT

production simulation using a 2-fs time-step at a temperature of 310 K, during which 500 trajectory points and 5,000 energy points were recorded. The trajectories from the final 50 ns of the simulation were extracted for further analysis.

The binding energy of Co^{2+} to the aptamer under different magnetic field conditions was calculated using the MMPBSA method. The total binding energy $E(total)$ was determined by

$$E_{total} = E_{gas} + E_{total} = (E_{vdw} + E_{electrostatic}) + (E_{GB} + E_{SA}) \quad (3)$$

where E_{gas} is the gas-phase energy, including van der Waals energy E_{vdw} and electrostatic interaction energy $E_{electrostatic}$, and E_{corr} is the solvent correction energy, which includes the Generalized-Born energy term E_{GB} and solvation area energy term E_{SA}.

GO-based fluorescence assays

FAM-labeled aptamers were heated at 95 ℃ for 10 min, cooled on ice for 10 min, and then placed at room temperature for 10 min. Binding affinity analysis was performed by incubating 25 nM of aptamers with a range of concentrations of target ions in a 400 μL volume for 30 min under either the ambient geomagnetic field or high magnetic fields. Then, the optimized amount of GO was added to the tube and incubated for 30 min under the magnetic field conditions described above. We measured the fluorescence intensity of the supernatants in a 96-well assay plate with a microplate reader (Thermo Varioskan Flash) after centrifugation at 15,173 x *g* for 3 min. In each affinity assay, the fluorescence intensity was normalized by establishing the maximal observed fluorescence intensity as a reference value of 1. The binding saturation curves and K_d were obtained through nonlinear regression analysis using Origin software.

Gel electrophoresis

We prepared the denatured aptamers as described above with different concentrations of the target. Unbound aptamers were removed by adsorption onto GO under either an ambient or 9 T magnetic field, and the supernatant was subjected to 12% PAGE. The relative intensities of the bands were calculated by ImageJ, and the saturation curves and K_d were obtained through nonlinear regression analysis with Origin software.

Isothermal titration calorimetry (ITC)

2 mM $CoCl_2$ and 20 μM aptamer were separately dissolved in binding buffer. Titration was performed using a MicroCal PEAQ-ITC with aptamers in the reaction cell and $CoCl_2$ in the injection syringe at 750 rpm at 25 ℃. The titration experiment consisted of 20 injections (2 μL, except for the first injection of 0.4 μL) with 200 s intervals between injections. The control experiment was conducted by incrementally introducing 2 mM $CoCl_2$ into the buffer without aptamers. Data were integrated and analyzed utilizing the MicroCal PEAQ-ITC Analysis Software.

Circular dichroism (CD) spectrometry

10 μM aptamer was dissolved in binding buffer. The aptamers were heated at 95 ℃ for 10 min, cooled on ice for 10 min, and then placed at room temperature for 10 min. The CD spectra were measured between 220–400 nm at 1 nm intervals and a speed of 200 nm/min using a 1-mm path-length fused quartz cell on a J1700 Circular Dichroism Spectropolarimeter (JASCO Ltd.). 100 μM Co^{2+} in binding buffer was then added to validate the structure change.

Kinetic binding analysis under high magnetic field

25 nM Co-M8 was mixed with 300 μM Co^{2+} in binding buffer. The reaction mixture was incubated within the bore of the 9 T superconducting magnet. Fluorescence intensity was monitored over a period of 0–60 min. At specific time intervals (2, 5, 10, 15, 20, 30, 40, 50, 60 min), 100 μg of GO was added to the tube and incubated for 30 min under the 9 T magnetic field. To capture the kinetic progression while minimizing post-incubation relaxation, aliquots were processed immediately at each time interval. We measured the fluorescence intensity of the supernatants in a 96-well assay plate with a microplate reader (Thermo Varioskan Flash) after centrifugation at 15,173 x *g* for 3 min.

Strand-displacement fluorescence assay

FAM-labeled aptamers were heated at 95 °C for 10 min, cooled on ice for 10 min, and then placed at room temperature for 10 min. Binding affinity analysis was performed by incubating 25 nM aptamer with a range of target ion concentrations in a 1 mL volume for 30 min under either ambient or high magnetic field. Subsequently, 10 μL of 5 μM 3'-BHQ1-labeled complementary DNA (cDNA, 20 nt) was added to the system and incubated for an additional 30 min. The 20-nt cDNA was designed to be complementary to the 5'-terminal primer binding region of the aptamer, positioned directly adjacent to the 5'-FAM label (sequence details are provided in Supplementary Table 4). Upon hybridization with the aptamer, the BHQ1 quencher significantly reduces the FAM fluorescence signal unless the aptamer is pre-stabilized in its folded state by the target ion. Immediately following incubation, samples were transferred for rapid fluorescence acquisition to minimize any post-incubation conformational changes. In each affinity assay, the fluorescence intensity was normalized by establishing the maximal observed fluorescence intensity as a reference value of 1. The binding saturation curves and K_d were obtained through nonlinear regression

analysis using Origin software.

FRET assay

The aptamer sequences (*i.e.,* Co-M3, Co-M8, and the initial library) were chemically synthesized with a fluorophore donor (FAM) at the 5'-end and a fluorescence acceptor (TAMRA) at the 3'-end. The dual-labeled aptamers were diluted to a final concentration of 100 nM in the binding buffer. To evaluate ion-induced conformational changes, the aptamer solutions were mixed with varying concentrations of Co^{2+} ranging from 0–300 μM. The samples were incubated for 30 min under either ambient or high magnetic field. Consistent with the above proposal, samples were then immediately transferred to a fluorescence spectrophotometer (Lengguang F97) for rapid measurement. The donor fluorophore was excited at 490 nm, and emission spectra were recorded from 500–650 nm. The FRET efficiency or fluorescence change was calculated based on the ratio of F_{580}/F_{518} emission intensities or the quenching efficiency of the donor.

UV-vis spectroscopic analysis

For nucleic acid conformational analysis (~260 nm), samples containing 2 μM aptamer (Co-M3 or Co-M8) and 20 μM Co^{2+} were used to monitor changes in the DNA absorbance band across the wavelength range of 220–350 nm. For metal coordination analysis (~500 nm), samples containing 200 μM aptamer and 2 mM Co^{2+} were used to detect the weak d–d transition bands of the Co^{2+} ions within the coordination pocket across the wavelength range of 420–800 nm. The samples were incubated for 30 min under either ambient or high magnetic fields. Immediately following incubation, samples were transferred to a UV-vis spectrophotometer (Thermo UV–10 s) for rapid spectral acquisition using a 1-cm quartz cuvette.

Specificity assay

25 nM of selected aptamers were incubated with target ions (300 μM for Co^{2+}, 30 μM for Hg^{2+}) or a 10-fold excess of interfering ions (including Mn^{2+}, Cu^{2+}, Ca^{2+}, Al^{3+}, Ba^{2+}, Cd^{2+}, Ni^{2+}, Zn^{2+}, Ce^{3+}, Pb^{2+}, Cr^{3+}, Fe^{3+}, Hg^{2+} or Co^{2+}) in 400 μL of the appropriate binding buffer. These assays were incubated for 30 min under ambient or high magnetic fields. After adding 50 μL of 2 mg/mL GO at room temperature, we continued the incubation under ambient or high magnetic fields for 30 min, centrifuged the mixtures at 15,173 x *g* for 5 min, and measured the fluorescence intensities of the supernatants using a microplate reader at an excitation wavelength of 485 nm and emission wavelength of 518 nm. The fluorescence intensity was normalized by defining the response values of Co^{2+} in a 9 T field as the reference unit with a magnitude of 1.

Chemical reactivity analysis of the Co^{2+} aptamer

2 μM FAM-labeled Co-M8 was prepared in 200 μL binding buffer alone or containing 300 μM Co^{2+}. The solution was heated to 90 °C for 5 min and then incubated for 60 min under ambient or high magnetic field to allow DNA structure formation.

For DMS reactivity (cleaving DNA at G), 200 μL of DNA was combined with 2 μL DMS and incubated at room temperature for 2 min. The reaction was quenched with 200 μL stop solution (1 M β-mercaptoethanol, 1 M Tris-OAc pH 7.5, 1.5 M NaOAc, 50 mM $Mg(OAc)_2$, and 1 mM EDTA), and then combined with 2 μL tRNA (10 mg/mL). Samples were supplemented with 1 mL pre-cooled anhydrous ethanol and centrifuged at 18,360 x *g* for 30 min. The DNA pellet was dried and resuspended in 60 μL of 1× PBS buffer (pH 7.4) containing 1 mM EDTA. Samples were heated to 90 °C for 20 min, cooled on ice for 10 min, and then 6 μL of 1 M NaOH was added, followed by incubation at 90 °C for 30 min. Samples

were then cooled to room temperature, mixed with 50 μL glycogen (5 mg/mL), and precipitated with anhydrous ethanol. The DNA pellets were washed with 250 μL of pre-cooled anhydrous ethanol (75%), air dried, and resuspended in 15 μL water. 45 μL deionized formamide was added to the samples, which were then incubated at 90 °C for 5 min to completely denature the DNA products.

For $KMnO_4$ reactivity (cleaving DNA at T), 200 μL DNA solution was mixed with 20 μL 160 mM $KMnO_4$ and incubated at room temperature for 5 min. The reaction was stopped by addition of 25 μL β-mercaptoethanol. Samples were then supplemented with 25 μL 500 mM EDTA and placed on ice, followed by precipitation with 1 mL pre-cooled anhydrous ethanol. The DNA pellets were air dried, resuspended in 300 μL piperidine (10%, v/v), heated to 90 °C for 25 min, and frozen on dry ice. Samples were then again precipitated with 1 mL anhydrous ethanol. DNA pellets were resuspended with 15 μL of water and 45 μL of deionized formamide and incubated at 90 °C for 5 min to denature the DNA products fully.

20 μL of the samples from DMS and $KMnO_4$ footprinting were subjected to electrophoresis with 16% denaturing PAGE gels (7.5 M urea) in 1× TBE running buffer for 5 h at 35 mA to allow band separation.

Statistics & Reproducibility

Most quantitative experiments were performed three independent times to ensure reproducibility. Data are presented as mean values ± SD, as indicated in the figure legends. The experiments shown in Fig. 2c, d; Fig. 3d, e; Fig. 6c, d; and Supplementary Figs. 2, 12-17, 18, 20, 21 were independently performed at least at least a duplicate of experiments, yielding consistent and reproducible results. Representative datasets are presented where appropriate. No statistical method was used to predetermine

sample size. No data were excluded. The experiments were not randomized. No blinding was required as the identity of each sample was known before each measurement.

Data Availability

All data needed to evaluate the conclusions in the paper are present in the paper and/or the Supplementary Materials. The high-throughput sequencing data generated in this study have been deposited in the NCBI Gene Expression Omnibus database under accession code PRJNA1395820 [https://www.ncbi.nlm.nih.gov/bioproject/PRJNA1395820]. The source data generated in this study are provided in the Source Data file.

References

1. Long, X., Ye, J., Zhao, D. & Zhang, S.-J. Magnetogenetics: remote non-invasive magnetic activation of neuronal activity with a magnetoreceptor. *Science Bulletin* **60**, 2107–2119 (2015).

2. Qin, S. *et al.* A magnetic protein biocompass. *Nature Mater* **15**, 217–226 (2016).

3. Meister, M. Physical limits to magnetogenetics. *eLife* **5**, e17210 (2016).

4. Winklhofer, M. & Mouritsen, H. A room-temperature ferrimagnet made of metallo-proteins? 094607 Preprint at https://doi.org/10.1101/094607 (2020).

5. Sigel, H. Interactions of metal ions with nucleotides and nucleic acids and their constituents. *Chem. Soc. Rev.* **22**, 255 (1993).

6. Sigel, R. K. O. & Sigel, H. A stability concept for metal ion coordination to single-stranded nucleic acids and affinities of individual sites. *Acc. Chem. Res.* **43**, 974–984 (2010).

7. Izatt, R. M., Christensen, J. J. & Rytting, J. H. Sites and thermodynamic quantities associated with proton and metal ion interaction with ribonucleic acid, deoxyribonucleic acid, and their constituent bases, nucleosides, and and nucleotides. *Chem. Rev.* **71**, 439–481 (1971).

8. Furukawa, K. *et al.* Bacterial Riboswitches Cooperatively Bind Ni^{2+} or Co^{2+} Ions and Control Expression of Heavy Metal Transporters. *Molecular Cell* **57**, 1088–1098 (2015).

9. Dambach, M. *et al.* The Ubiquitous yybP-ykoY Riboswitch Is a Manganese-Responsive Regulatory Element. *Molecular Cell* **57**, 1099–1109 (2015).

10. Price, I. R., Gaballa, A., Ding, F., Helmann, J. D. & Ke, A. Mn^{2+}-sensing mechanisms of yybP-ykoY orphan riboswitches. *Molecular Cell* **57**, 1110–1123 (2015).

11. Xu, T. *et al.* Small DNAs that Bind Nickel(II) Specifically and Tightly. *Anal. Chem.* **93**, 14912–14917 (2021).

12. Wu, Y. *et al.* Simultaneous Fe^{2+}/Fe^{3+} imaging shows Fe^{3+} over Fe^{2+} enrichment in Alzheimer's disease mouse brain. *Sci. Adv.* **9**, eade7622 (2023).

13. Wrzesinski, J. & Ciesiolka, J. Characterization of Structure and Metal Ions Specificity of Co^{2+}-Binding RNA Aptamers. *Biochemistry* **44**, 6257–6268 (2005).

14. Nishiyabu, R. *et al.* Nanoparticles of adaptive supramolecular networks self-assembled from nucleotides and lanthanide ions. *J. Am. Chem. Soc.* **131**, 2151–2158 (2009).

15. Tsitovich, P. B., Spernyak, J. A. & Morrow, J. R. A Redox-Activated MRI Contrast Agent that Switches Between Paramagnetic and Diamagnetic States. *Angew Chem Int Ed* **52**, 13997–14000 (2013).

16. Gale, E. M., Jones, C. M., Ramsay, I., Farrar, C. T. & Caravan, P. A Janus Chelator Enables Biochemically Responsive MRI Contrast with Exceptional Dynamic Range. *J. Am. Chem. Soc.* **138**, 15861–15864 (2016).

17. Zakharchenko, A., Guz, N., Laradji, A. M., Katz, E. & Minko, S. Magnetic field remotely controlled selective biocatalysis. *Nat Catal* **1**, 73–81 (2017).

18. Liu, X. *et al.* Magnetic-field-oriented mixed-valence-stabilized ferrocenium anion-exchange membranes for fuel cells. *Nat Energy* **7**, 329–339 (2022).

19. Rangel, A. E., Hariri, A. A., Eisenstein, M. & Soh, H. T. Engineering Aptamer Switches for Multifunctional Stimulus-Responsive Nanosystems. *Advanced Materials* **32**, 2003704 (2020).

20. Zhu, H. *et al.* Spatial control of in vivo CRISPR–Cas9 genome editing via nanomagnets. *Nat Biomed Eng* **3**, 126–136 (2018).

21. Park, J.-W., Tatavarty, R., Kim, D. W., Jung, H.-T. & Gu, M. B. Immobilization-free screening of aptamers assisted by graphene oxide. *Chem. Commun.* **48**, 2071–2073 (2012).

22. Stangherlin, S., Lui, N., Lee, J. H. & Liu, J. Aptamer-based biosensors: from SELEX to biomedical diagnostics. *TrAC Trends in Analytical Chemistry* **191**, 118349 (2025).

23. Shi, H. *et al.* Selection and application of DNA aptamers against sulfaquinoxaline assisted by graphene oxide–based SELEX. *Food Anal. Methods* **14**, 250–259 (2021).

24. Wang, J. *et al.* A general transition metal binding aptamer following the Irving–Williams series. *Chem. Sci.* **16**, 14286–14294 (2025).

25.Alkhamis, O. *et al.* Exploring the relationship between aptamer binding thermodynamics, affinity, and specificity. *Nucleic Acids Res* **53**, gkaf219 (2025).

26. Slavkovic, S. & Johnson, P. E. Analysis of Aptamer-Small Molecule Binding Interactions Using Isothermal Titration Calorimetry. in *Nucleic Acid Aptamers* (eds Mayer, G. & Menger, M. M.) vol. 2570 105–118 (Springer US, New York, NY, 2023).

27. Cowan, J. A. Recognition of a cognate RNA aptamer by neomycin B: quantitative evaluation of hydrogen bonding and electrostatic interactions. *Nucleic Acids Res* **28**, 2935–2942 (2000).

28. Black, C. B. & Cowan, J. A. Quantitative Evaluation of Electrostatic and Hydrogen-Bonding Contributions to Metal Cofactor Binding to Nucleic Acids. *J. Am. Chem. Soc.* **116**, 1174–1178 (1994).

29. Ding, Y., Heng, Y., Wong, K., Chen, Q. & Liu, J. Enriching Higher Affinity Aptamers by Addressing the Kinetic Aspect of the DNA Strand-Displacement Reaction. *Angew Chem Int Ed* **n/a**,

e14445 (2025).

30. Aich, P. *et al.* M-DNA: a complex between divalent metal ions and DNA which behaves as a molecular wire. *Journal of Molecular Biology* **294**, 477–485 (1999).

31. Lee, J. S., Latimer, L. J. P. & Reid, R. S. A cooperative conformational change in duplex DNA induced by Zn^{2+} and other divalent metal ions. *Biochem. Cell Biol.* **71**, 162–168 (1993).

32. Bailey, T. L. *et al.* MEME SUITE: tools for motif discovery and searching. *Nucleic Acids Res* **37**, W202–W208 (2009).

33. Hou, T., Wang, J., Li, Y. & Wang, W. Assessing the Performance of the MM/PBSA and MM/GBSA Methods. 1. The Accuracy of Binding Free Energy Calculations Based on Molecular Dynamics Simulations. *J. Chem. Inf. Model.* **51**, 69–82 (2011).

34. Zhou, M. *et al.* Small DNAs that specifically and tightly bind transition metal ions. *J. Am. Chem. Soc.* **145**, 8776–8780 (2023).

35. Smestad, J., Wilbanks, B. & Maher, L. J. An in Vitro Selection Strategy Identifying Naked DNA That Localizes to Cell Nuclei. *J. Am. Chem. Soc.* **141**, 18375–18379 (2019).

36. Chen, H. *et al.* Exploring the formation and recognition of an Important G-Quadruplex in a HIF1α promoter and its transcriptional inhibition by a Benzo[*c*]phenanthridine derivative. *J. Am. Chem. Soc.* **136**, 2583–2591 (2014).

37. McManus, S. A. & Li, Y. A Deoxyribozyme with a Novel Guanine Quartet-Helix Pseudoknot Structure. *Journal of Molecular Biology* **375**, 960–968 (2008).

38. Mao, Y. *et al.* Evolution of a highly functional circular DNA aptamer in serum. *Nucleic Acids Res.* **48**, 10680–10690 (2020).

39. Zhou, W., Saran, R. & Liu, J. Metal Sensing by DNA. *Chem. Rev.* **117**, 8272–8325 (2017).

40. Xu, J. *et al.* Magnetic sensitivity of cryptochrome 4 from a migratory songbird. *Nature* **594**, 535–540 (2021).

41.Li, J. H. *et al.* Directed manipulation of membrane proteins by fluorescent magnetic nanoparticles. *Nat Commun* **11**, 4259 (2020).

42. Jiang, H., Fu, H., Min, T., Hu, P. & Shi, J. Magnetic-Manipulated NK Cell Proliferation and Activation Enhance Immunotherapy of Orthotopic Liver Cancer. *J. Am. Chem. Soc.* **145**, 13147–13160 (2023).

43. Liu, W. *et al.* Remote Tuning of Built-In Magnetoelectric Microenvironment to Promote Bone

Regeneration by Modulating Cellular Exposure to Arginylglycylaspartic Acid Peptide. *Adv Funct Materials* **31**, 2006226 (2021).

44. Lee, J. *et al.* Non-contact long-range magnetic stimulation of mechanosensitive ion channels in freely moving animals. *Nat. Mater.* **20**, 1029–1036 (2021).

45. Greenberg, B. D., Ziemann, U., Harmon, A., Murphy, D. L. & Wassermann, E. M. Decreased neuronal inhibition in cerebral cortex in obsessive compulsive disorder on transcranial magnetic stimulation. *The Lancet* **352**, 881–882 (1998).

46. Stanley, S. A., Sauer, J., Kane, R. S., Dordick, J. S. & Friedman, J. M. Remote regulation of glucose homeostasis in mice using genetically encoded nanoparticles. *Nat Med* **21**, 92–98 (2015).

47. Chen, Y. *et al.* Plasmonic/magnetic nanoarchitectures: From controllable design to biosensing and bioelectronic interfaces. *Biosensors and Bioelectronics* **219**, 114744 (2023).

48. Zuker, M. Mfold web server for nucleic acid folding and hybridization prediction. *Nucleic Acids Res* **31**, 3406–3415 (2003).

49. Wang, J. *et al.* Optimization of RNA 3D structure prediction using evolutionary restraints of nucleotide–nucleotide interactions from direct coupling analysis. *Nucleic Acids Res* **45**, 6299–6309 (2017).

50. Wang, J., Wang, J., Huang, Y. & Xiao, Y. 3dRNA v2.0: An Updated Web Server for RNA 3D Structure Prediction. *IJMS* **20**, 4116 (2019).

51. Zhang, Y., Jiang, Y., Peng, J. & Zhang, H. Rational Design of Nonbonded Point Charge Models for Divalent Metal Cations with Lennard-Jones 12-6 Potential. *J. Chem. Inf. Model.* **61**, 4031–4044 (2021).

52. Plimpton, S. Fast Parallel Algorithms for Short-Range Molecular Dynamics. *Journal of Computational Physics* **117**, 1–19 (1995).

Acknowledgements

This work was supported by the National Natural Science Foundation of China (U23A20265, 32072306 to L.Z.), and the Anhui Provincial Natural Science Foundation (2408085MC072 to L.W.). We thank the staff members of the SM1 superconducting magnet (https://cstr.cn/31125.02.SHMFF.SM1.MG) at the Steady High Magnetic Field Facility, CAS (https://cstr.cn/31125.02.SHMFF), for providing technical support and assistance. The analysis work of this article was partially carried out at the Instrumental Analysis Center, Hefei University of Technology.

Author Contributions Statement

Conceptualization: L.W., H.T.S. and L.Z. Methodology: S.G., L.W., Y.M., H.T.S. and L.Z. Investigation and Validation: S.G. and L.Y. Visualization: S.G. Data Curation: S.G. and L.Y. Formal analysis: S.G. and L.W. Resources: L.W., Y.M., and L.Z. Writing - Original Draft: S.G. and L.W. Writing - Review & Editing: S.G., L.W., M.E., H.T.S. and L.Z. Supervision, Project administration: L.W., H.T.S. and L.Z. Funding acquisition: L.W. and L.Z. All authors have read and agreed to the submitted version of the manuscript.

Competing Interests Statement

S. G., L. W., and L. Z. are inventors on a patent granted to Hefei University of Technology related to the screening of magnetic-sensitive aptamers for Co^{2+} (application number 202510331988.8). The remaining authors declare no competing interests.

Figure Legends

Figure 1 Schematic illustration of HM-SELEX. The HM-SELEX screening process is based on the GO-SELEX methodology and combines both positive- and counter-SELEX approaches. Positive SELEX (left) is performed using a steady 9 T magnetic field generated by a superconducting magnet, with unbound sequences removed via adsorption of single-stranded DNA onto graphene oxide (GO). The counter-SELEX process (right) involves three sequential steps: using GO binding to remove DNA sequences that bind to counter-targets under a 9 T field, using GO binding to eliminate sequences that bind the target under the ambient geomagnetic field ($\leq 5\times10^{-5}$ T), and finally, recovering target-binding sequences under the 9 T field after using GO to remove unbound sequences.

Figure 2 Analysis of aptamers that exhibit improved Co^{2+} affinity under high magnetic field. a, Five of our 10 most abundant sequences exhibited significantly improved affinity under a 9 T field relative to the ambient geomagnetic field. (Data are presented as mean ± standard deviation (SD). Each bar represents an independent sequence (n = 3 replicates). **b**, The affinity shift of Co-M3 under various magnetic fields. Binding curves and K_d values were obtained by nonlinear regression analysis with Origin software. The inset shows actual fluorescence of the samples. For all relevant panels, data are shown as mean ± SD. (n = 3 replicates). **c**, Isothermal titration calorimetry (ITC) thermograms and integrated heat of titrating 2 mM Co^{2+} into 20 μM Co-M3 under ambient magnetic conditions. Binding experiments were performed at 25 °C in buffer containing 50 mM HEPES, 100 mM NaCl, 0.025% Tween-20 (pH 7.5). **d**, Circular dichroism (CD) spectra of 10 μM Co-M3 before and after adding 100 μM Co^{2+} under ambient magnetic conditions. Source data are provided as a Source Data file.

Figure 3 Analysis of aptamers that only bind to Co^{2+} under a high magnetic field. a, Fluorescence response of Co-M8 to 300 μM Co^{2+} at 9 T or ambient magnetic conditions. Inset shows actual fluorescence of the samples. **b**, Affinity shift of Co-M8 under ambient conditions or magnetic fields. **c**, Binding of Co-M10 to Co^{2+} under ambient or 9 T magnetic field. For all relevant panels, data are shown as mean ± SD. (n = 3 replicates). **d**, ITC thermograms and integrated heat of titrating 2 mM Co^{2+} into 20 μM Co-M8 under ambient conditions. Binding experiments were performed at 25 °C in buffer containing 50 mM HEPES, 100 mM NaCl, 0.025% Tween-20 (pH 7.5). **e**, CD spectra of 10 μM Co-M8 before and after adding 100 μM Co^{2+} under ambient conditions. Source data are provided as a Source Data file.

Figure 4 Specificity of the selected Co^{2+} aptamers against non-target ions. a, Binding of Co-M3 and **b**, Co-M8 to 300 μM Co^{2+} or 3 mM of various non-target ions under ambient or 9 T magnetic field. Data are presented as mean ± SD (n = 3 replicates) with individual data points overlaid on the bars. Source data are provided as a Source Data file.

Figure 5 Cluster analysis and secondary structure of enriched sequences that bind to Co^{2+}. a, Design of the initial Co-library (top) and the 10 most abundant sequences in the final Co-binding pool (bottom). Colored regions represent conserved nucleotides of motifs M1 (red), M2 (orange), and M3 (green). **b**, Sequence logos for motifs M1, M2, and M3. **c–e**, Mfold-predicted secondary structure of Co-M3 (**c**), -M5 (**d**), and -M8 (**e**). Source data are provided as a Source Data file.

Figure 6 MD simulations of Co^{2+} binding under high magnetic field. a, **b**, Three-dimensional conformations of **(a)** Co-M3 and (**b**) -M8 bound to Co^{2+} under varying magnetic field conditions. **c**, **d**, Interaction energy profiles of (**c**) Co-M3 and (**d**) -M8 binding to Co^{2+} under various magnetic field conditions. **e**, **f**, Interaction map of key regions within the binding pocket of Co^{2+} in (**e**) Co-M3 and (**f**) -M8 under a 9 T magnetic field. Source data are provided as a Source Data file.

Figure 7 Mutagenesis analysis of Co-M8. a, We performed targeted point-mutagenesis of Co-M8 at the purple nucleotides, and evaluated these mutants in terms of their K_d for Co^{2+} under ambient or 9 T magnetic fields. **b**, Analysis of key secondary structure features contributing to affinity shifts. **c**, Affinity shift of Co-M8 mutants at a 9 T magnetic field. Data are presented as mean ± SD (n = 3 replicates) with individual data points overlaid on the bars. Source data are provided as a Source Data file.

Editorial summary:

While magnetic fields present a compelling avenue for the remote control of molecular recognition, few direct strategies currently exist. Here, authors generate DNA aptamers whose affinity for Co2+ can be switched on or enhanced by magnetic field, thereby potentially enabling remote control of biorecognition.

Peer review information: *Nature Communications* thanks Hongzhou Gu, and the other, anonymous, reviewer(s) for their contribution to the peer review of this work. A peer review file is available.

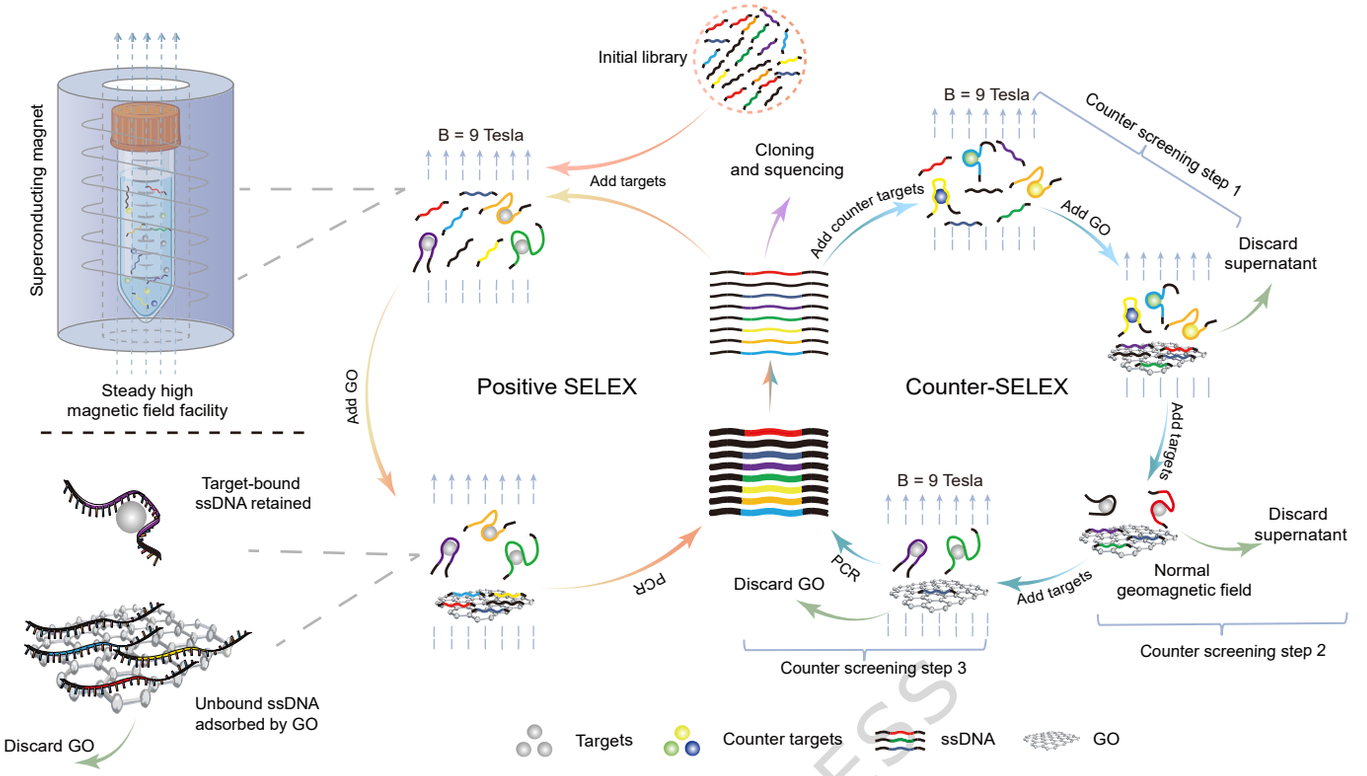

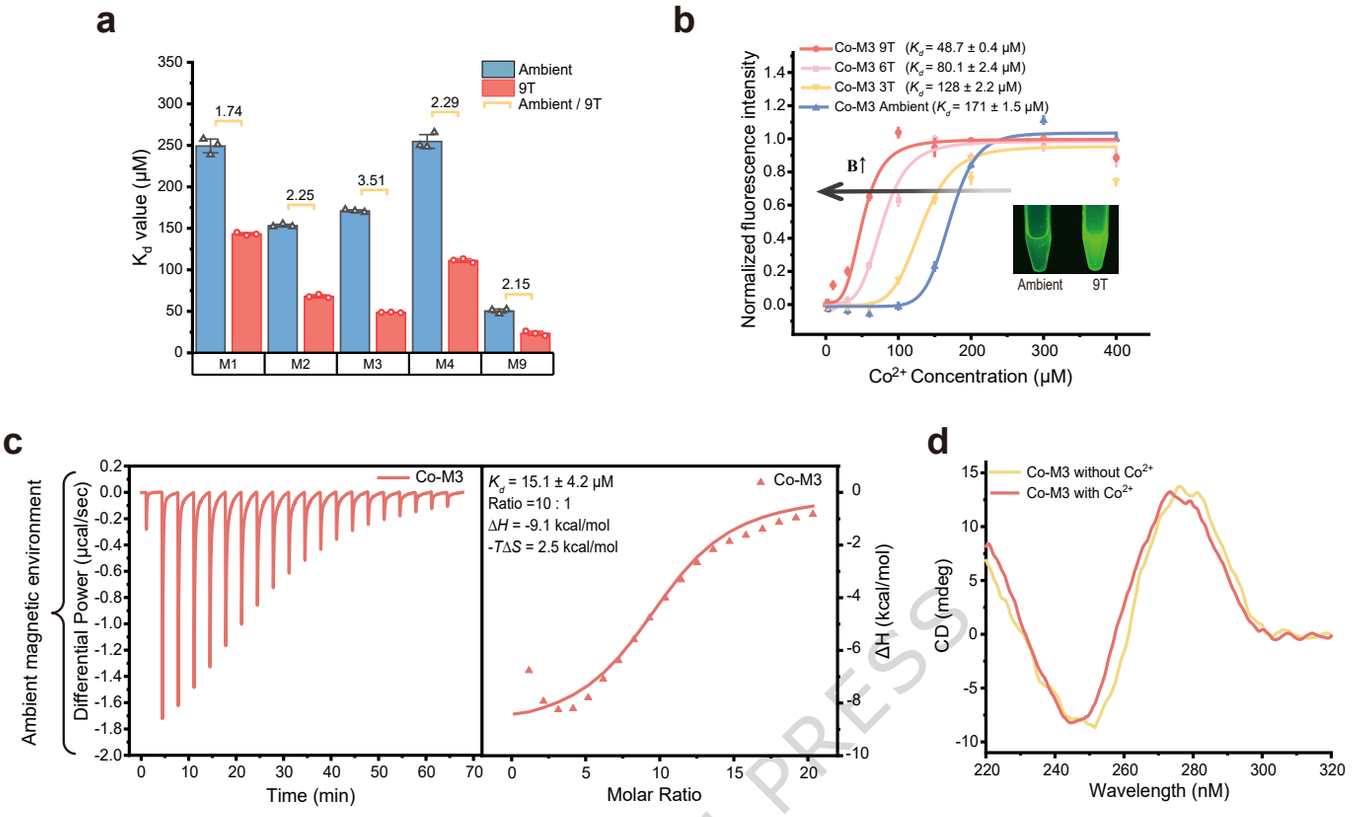

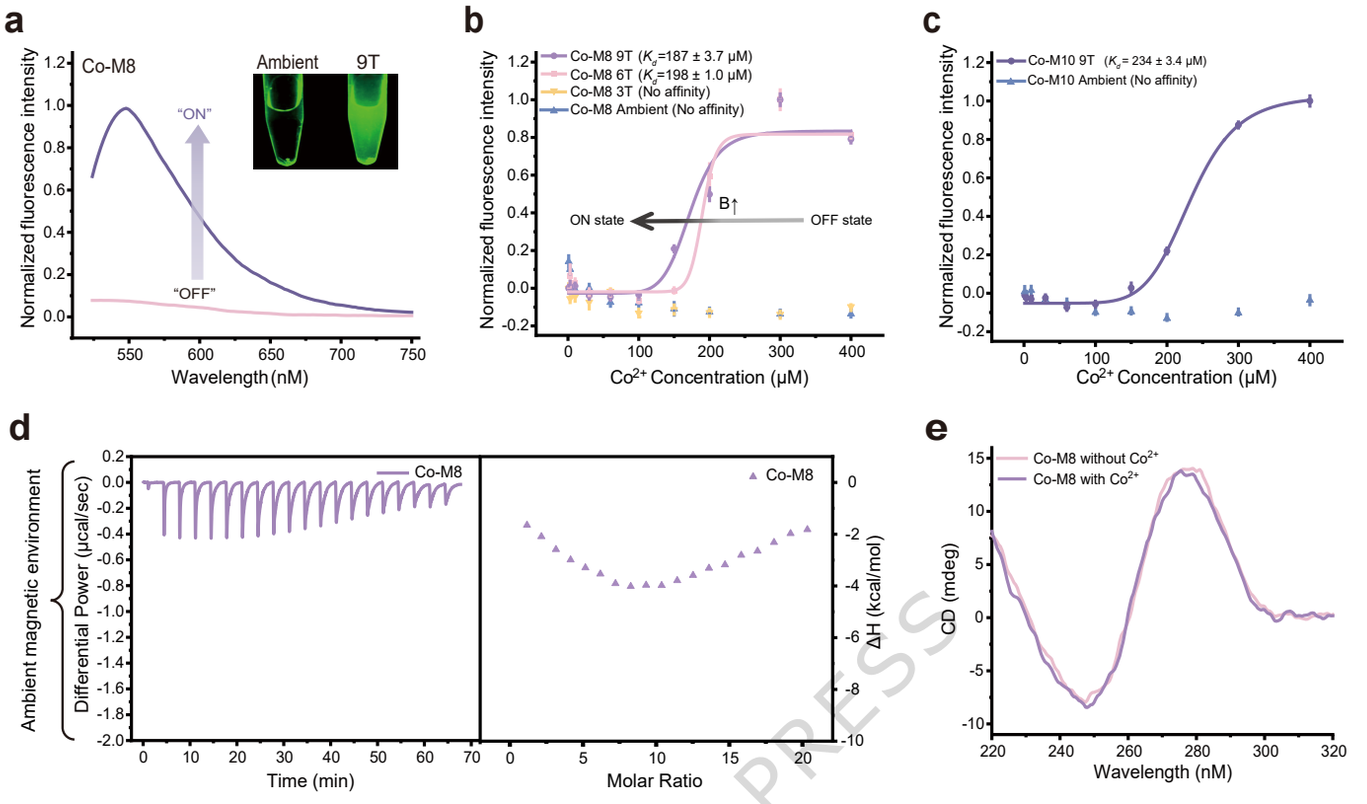

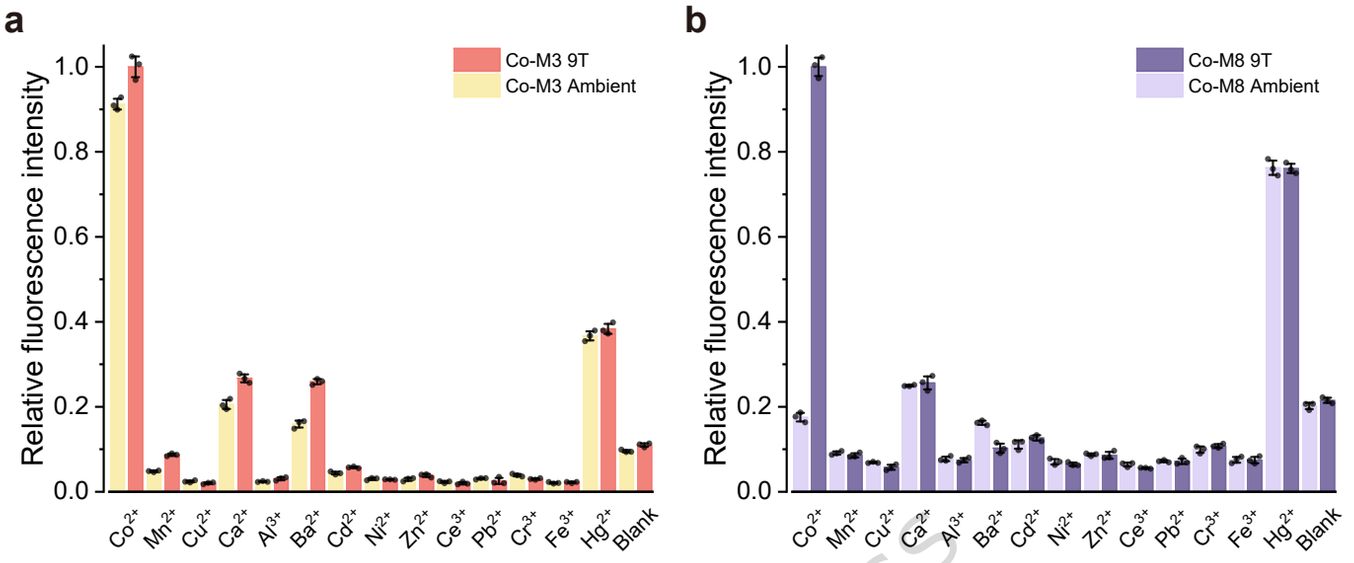

a

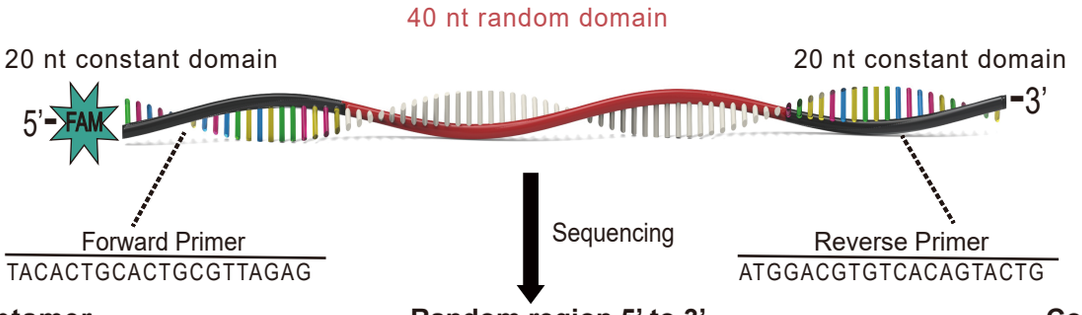

Co-aptamer	Random region 5' to 3'	Copies
Co-M1	...ATTACGTCCCTTGCTCCTCTTTAAATGGCCGCAGGTTACG...	8513
Co-M2	...ATTACGTCCGGCTTTATGCCCTCCTTTGACACTGTTAACG...	3521
Co-M3	...GTTACGGCCCCTGCTCAGCACAGCTCCTTTATGGTATACG...	2841
Co-M4	...ATTACGGCCCCATGCTCCAAGAGACCAAAGGTCATTAACG...	2695
Co-M5	...CTACGGCCCGGATTTTCCGCTACTTTGTCTATTTGATCGG...	2691
Co-M6	...GTCTACGGCCATTTTTTTCCTCTGCGACGCACTTGTTACGG...	2553
Co-M7	...CTGCGTCCCTTGCTGTTCCTTGACACCCGAAGGGTAACGG...	2203
Co-M8	...CTCTACGTCCATGGTTCCCAGCTCGAATTCTCTTTAACGG...	2158
Co-M9	...ATTACGGCCTGTGCCCTAGGGCACACTCTCTTTGGCAACG...	2158
Co-M10	...ATTACGTCCCTTGCTCCTTAAGTCCCGTAGTCGGGTTCCG...	1997

b

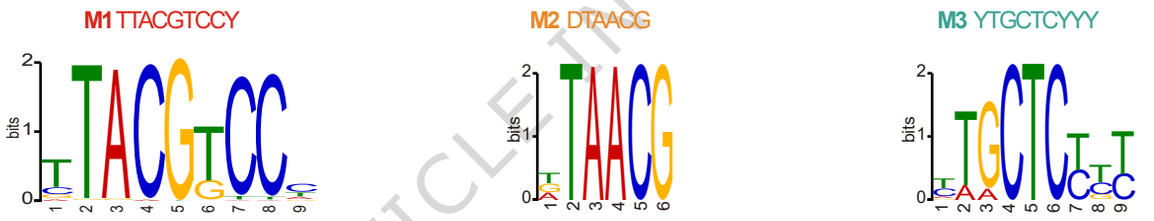

c

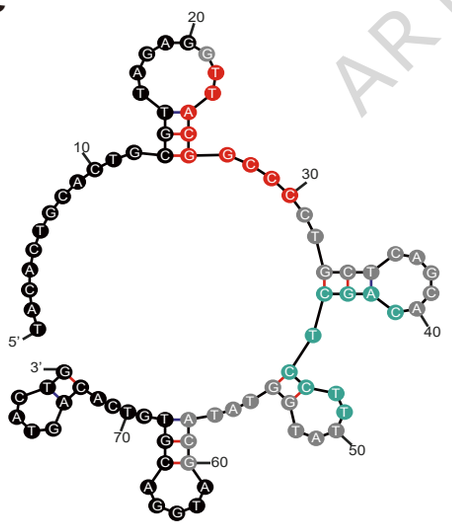

Co-M3

d

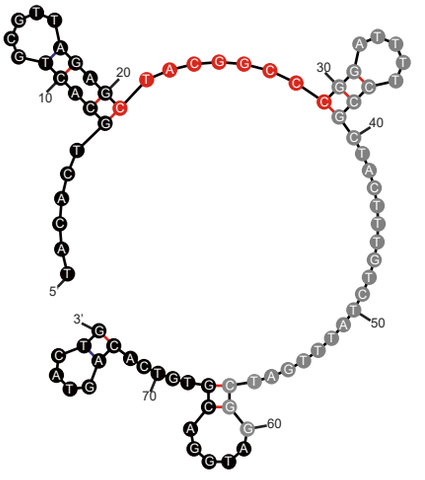

Co-M5

e

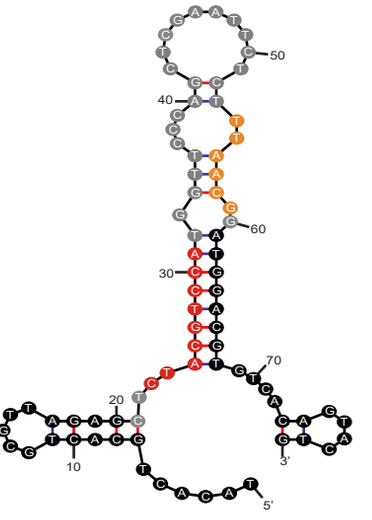

Co-M8

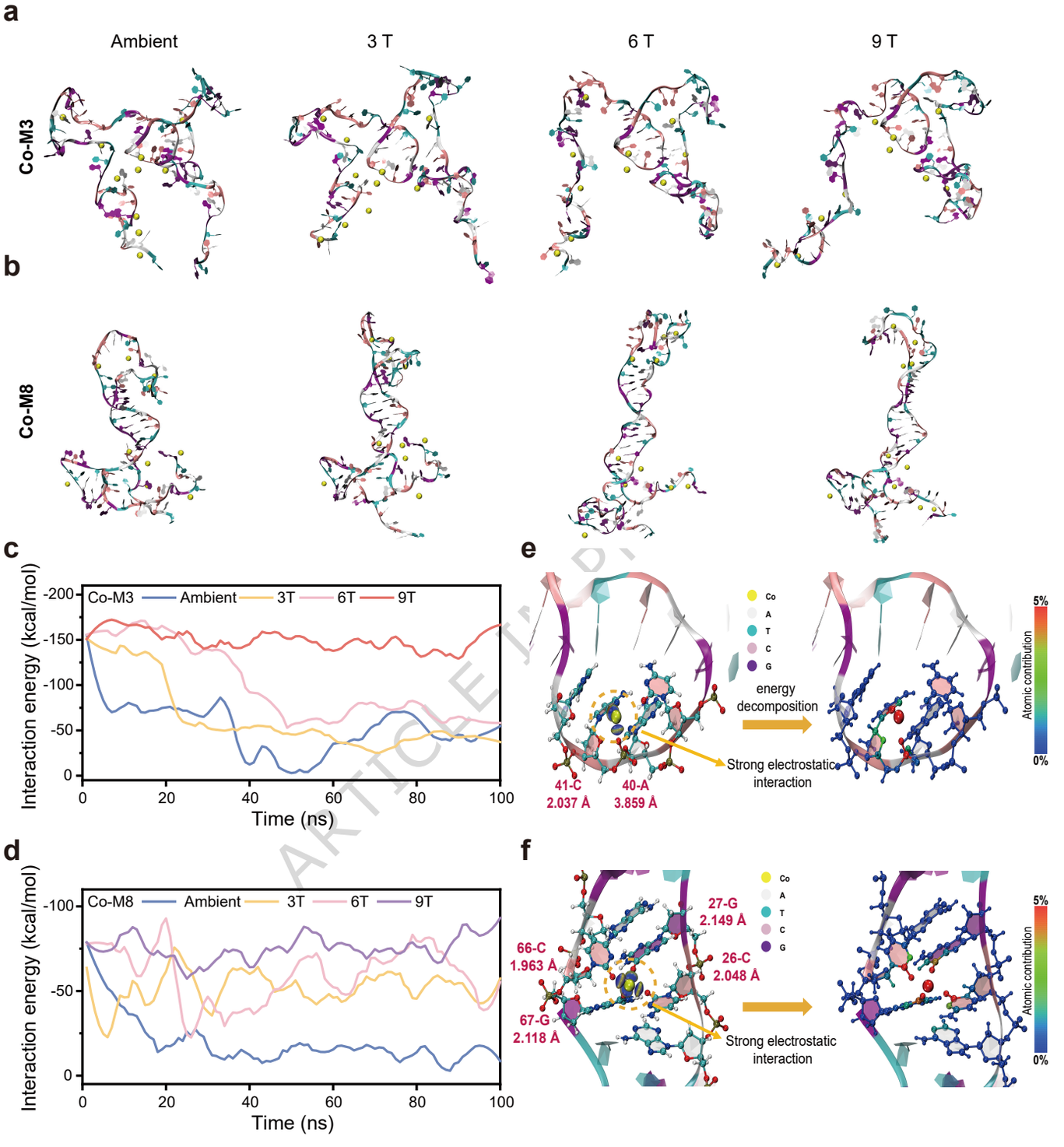
a
Ambient
3 T
6 T
9 T
Co-M3
b
Co-M8
c
Co-M3 Ambient 3T 6T 9T
Interaction energy (kcal/mol)
Time (ns)
d
Co-M8 Ambient 3T 6T 9T
Interaction energy (kcal/mol)
Time (ns)
e
Co
A
T
C
G
energy decomposition
Strong electrostatic interaction
41-C 2.037 Å
40-A 3.859 Å
Atomic contribution
5%
0%
f
27-G 2.149 Å
66-C 1.963 Å
26-C 2.048 Å
67-G 2.118 Å
Strong electrostatic interaction
Atomic contribution
5%
0%

a

Name	Sequence 5' to 3'	K_d (μM) Ambient	9T
Co-M8	TACAC TGCAC TGCGT TAGAG CTCTA CGTCC ATGGT TCCCA GCTCG AATTC TCTTT AACGG ATGGA CGTGT CACAG TACTG	NA	187
Co-M8-C26G	TACAC TGCAC TGCGT TAGAG CTCTA GGTCC ATGGT TCCCA GCTCG AATTC TCTTT AACGG ATGGA CGTGT CACAG TACTG	NA	NA
Co-M8-G27T	TACAC TGCAC TGCGT TAGAG CTCTA CTTCC ATGGT TCCCA GCTCG AATTC TCTTT AACGG ATGGA CGTGT CACAG TACTG	NA	NA
Co-M8-T35A	TACAC TGCAC TGCGT TAGAG CTCTA CGTCC ATGGA TCCCA GCTCG AATTC TCTTT AACGG ATGGA CGTGT CACAG TACTG	NA	NA
Co-M8-T36A	TACAC TGCAC TGCGT TAGAG CTCTA CGTCC ATGGT ACCCA GCTCG AATTC TCTTT AACGG ATGGA CGTGT CACAG TACTG	NA	NA
Co-M8-C52T	TACAC TGCAC TGCGT TAGAG CTCTA CGTCC ATGGT TCCCA GCTCG AATTC TTTTT AACGG ATGGA CGTGT CACAG TACTG	205	66.0
Co-M8-T53C	TACAC TGCAC TGCGT TAGAG CTCTA CGTCC ATGGT TCCCA GCTCG AATTC TCCTT AACGG ATGGA CGTGT CACAG TACTG	194	61.0
Co-M8-G63T	TACAC TGCAC TGCGT TAGAG CTCTA CGTCC ATGGT TCCCA GCTCG AATTC TCTTT AACGG ATTGA CGTGT CACAG TACTG	NA	NA
Co-M8-G64A	TACAC TGCAC TGCGT TAGAG CTCTA CGTCC ATGGT TCCCA GCTCG AATTC TCTTT AACGG ATGAA CGTGT CACAG TACTG	NA	NA